Journal Name

ARTICLE

A Comparative Study of Metal (Ni, Co, or Mn)-Borate Catalysts and Their Photodeposition on rGO/ZnO Nanoarrays for Photoelectrochemical Water Splitting

Received 00th January 20xx,
Accepted 00th January 20xx

DOI: 10.1039/x0xx00000x

www.rsc.org/

Huayang Zhang,[‡ab] Wenjie Tian,[‡a] Yunguo Li,[‡c] Hongqi Sun,*[b] Moses O. Tadé[a] and Shaobin Wang*[a]

Feasible and efficient photoelectrochemical (PEC) water splitting demands a rational integration of solar light absorbers with active electrocatalysts. Herein, we first compare three amorphous metal-borates (M-Bi, M = Ni, Co, Mn) as low-cost electrocatalysts, among which Mn-Bi is proposed for the first time for fabrication of new PEC devices for oxygen evolution reaction (OER). Density functional theory (DFT) calculations compared the catalytic activity of the effective structures in M-Bi and found that NiO_6 possesses kinetically the lowest overall OER energy barrier. Experimentally, M-Bi thin layers were self-assembled on reduced graphene oxide (rGO) linked ZnO nanorod arrays respectively, to form highly efficient ternary PEC system (M-Bi/rGO/ZnO) using a modified photodeposition method. rGO facilitates the fast charge separation in light-absorbing ZnO NAs, while M-Bi (M = Ni, Co, Mn) can improve the kinetics of OER. In accordance with DFT results, Ni-Bi serves as the most active electrocatalyst in such a PEC device, followed by Co-Bi and Mn-Bi. Compared to ZnO, the photoelectroconversion efficiency is elevated by approximately 4 times on Ni-Bi/rGO/ZnO, with its onset potential migrated by 0.17 V in the cathodic direction under one-sun illumination.

1. Introduction

Sunlight provides the Earth with plentiful energy and is by far the largest renewable energy resource. Substantial interests have been focused on this energy, especially when fossil fuels are being increasingly depleted. In the harvest and storage of solar energy, splitting water into hydrogen and oxygen seems to be an attractive option. Through this process, solar energy is captured and stored in the produced clean hydrogen, which can be readily combusted to release energy with the by-product of water.[1,2] In recent years, artificial photosynthesis via a photoelectrochemical (PEC) solar-to-hydrogen process has received particular attention, which is the most efficient coupling process of sunlight irradiation with electrochemical devices.[3,4] In this case, considerable studies have been targeting the development of an efficient electrocatalyst/light-harvest electrode system,[5] where a semiconductor with suitable stability and light absorption serves as a light-harvester, while the electrocatalyst is generally deposited on the top of the semiconductors to reduce the overpotential in hydrogen evolution reaction (HER) and oxygen evolution reaction (OER).[6]

Compared to HER, OER half-reaction (also known as water oxidation) is the rate-limiting step for water splitting as it is kinetically more-demanding by conducting the $4e^- - 4H^+$ proton-coupled electron transfer (PCET) process, imposing higher OER overpotentials.[7,8] Therefore, efficient OER electrocatalysts are critical for achieving excellent PEC water splitting performances. Despite of superior OER activities, noble metal oxides (e.g. RuO_2 or IrO_2) as electrocatalysts are economically unviable, due to the high cost. Driven by pursuing a wide availability and low cost, special attention has been given to the earth-abundant transition metals as well as their compounds.[9,10] The majority of OER electrocatalysts usually works best in basic media (pH 13-14), in which the charge carrier concentration is the greatest. However, neutral or milder pH electrolytes are desired because most of semiconductors degrade rapidly in extreme pH regimes. In addition, mild pH environment is beneficial for a long-term performance of the device with a slow degradation rate and less leakage.[11] In this regard, amorphous thin-film OER catalysts have been self-assembled by photo- or electro-deposition from transition-metal solutions (e.g. aqueous Co^{2+} and Ni^{2+}) in the presence of a buffering electrolyte, for example, phosphate (Pi), borate (Bi), or methylphosphonate (MePi), and they exhibit

[a] WA School of Mines: Minerals, Energy and Chemical Engineering, Curtin University, GPO Box U1987, WA 6845, Australia. E-mail: shaobin.wang@curtin.edu.au
[b] School of Engineering, Edith Cowan University, 270 Joondalup Drive, Joondalup, WA 6027, Australia. E-mail: h.sun@ecu.edu.au
[c] Department of Earth Sciences, University College London, Gower Street, London WC1E 6BT, United Kingdom.
‡ These authors contributed equally.
Electronic Supplementary Information (ESI) available: [details of any supplementary information available should be included here]. See DOI: 10.1039/x0xx00000x

high OER activities at pH 7-9.[12–15] Attributed to the borate or phosphate, these oxygen evolution catalysts (OECs) have a superior self-healing capability to compensate catalyst corrosion and operate steadily with high activities.[16,17] Moreover, they can be *in situ* interfaced with light absorbers to construct novel artificial-leaf-like architectures for enhanced PEC water splitting.[18–21] Some studies have reported such OER catalyst films using Co-Bi, Co-Pi, Ni-Pi, and Mn-Pi layers.[17,18,21,22] However, it lacks a comprehensive comparison in terms of the OER activity of these transition-metal-based thin films, which could be important to prepare more efficient OECs for electrocatalytic or PEC applications.

Herein, we first present a systematic investigation of Ni-, Co-, or Mn- Bi based OECs by both theoretical studies and experiments. Density functional theory (DFT) calculations were conducted to compare the OER kinetics of the active structures in Ni-Bi, Co-Bi and Mn-Bi catalysts. Then, M-Bi were adopted as efficient OECs for construction of electrocatalyst/light-harvester PEC device to compare their OER activity experimentally. To construct this device, ZnO at a low cost and high electron mobility was selected as the target photoabsorber. It is believed that a well-aligned one-dimensional (1D) configuration endows the semiconductor with high surface-to-volume ratios and provides an axial length transport pathway for carriers to reduce their recombination rate.[22,23] Accordingly, vertically aligned 1D ZnO nanorod arrays (NAs) were grown onto fluorine-doped tin oxide (FTO) glass following the method reported in ref. [24] with modifications of heating time and temperature. Noticeably, due to its superior electron mobility and high specific surface area, rGO has been widely introduced to improve the charge separation efficiency of photocatalysts.[22] Therefore, rGO was further loaded onto ZnO NAs in this work to enhance the conductivity, inhibit electron-hole recombination and promote charge separation on ZnO, as revealed by previous DFT calculations.[25] Finally, amorphous thin films of M-Bi (M = Ni, Co, Mn) were photo-deposited onto the rGO/ZnO NAs. Noteworthy, Mn-Bi is proposed for the first time for OER application. It is also noticed that most studies prepared M-Bi, or metal-phosphonate (M-Pi) films using the electrodeposition method while the reports on photochemical deposition are much less. Interestingly, photochemical deposition has its advantage over electrodeposition for the photo-related applications, because OECs tend to deposit on the locations enriched with photo-generated holes.[12] This ensures the most efficient use of OECs, resulting in enhanced photochemical O_2 evolution.[26] As a result, Ni-Bi/rGO/ZnO, Co-Bi/rGO/ZnO, and Mn-Bi/rGO/ZnO photoanodes were fabricated, which have not been reported elsewhere. The activity of M-Bi in improving OER kinetics of photoabsorbers can be experimentally compared by PEC-OER tests on these photoanodes. We hope that this endeavor will provide guiding principles for rational construction of artificial photosynthesis systems.

2. Experimental section

The details of DFT calculation methods and material characterizations are provided in Supporting Information.

2.1. Chemical reagents

Zinc acetate (99.99%), zinc nitrate hexahydrate (≥ 99%), hexamethylenetetramine (≥ 99%), boric acid (≥ 99.5%), potassium hydroxide (≥ 85%), nickel nitrate hexahydrate (≥ 98.5%), manganese nitrate tetrahydrate (≥ 97%), and cobalt chloride (≥ 98%) were received from Sigma-Aldrich and used without purification.

2.2. Preparation of ZnO and rGO/ZnO

ZnO was successfully grown on F-doped SnO_2 (FTO) glass (1×1.5 cm^2) according to a seed assisted method,[24] with modified heating time and temperature. Briefly, 100 mL of 0.06 M zinc acetate solution (dissolved in ethanol) was spin-coated onto the pretreated FTO substrate and annealed at 350 °C in air for 30 min to form ZnO seeds. Then, the FTO substrate was immersed in a mixed 60 mL solution of zinc nitrate hexahydrate (30 mM) and hexamethylenetetramine (HMT, 30 mM), which was transferred into a Teflon-lined autoclave and heated at 110 °C for 12 h. Finally, the resulting ZnO arrays grown on FTO were washed by distilled water and dried. For the preparation of rGO/ZnO composites, graphite oxide (GO) prepared via a modified Hummers method was used.[27] The GO aqueous solution (0.2 mg mL^{-1}) was spin-coated onto the prepared ZnO NAs for 5 times, followed by an annealing process at 450 °C for 2 h in N_2 atmosphere, where GO was thermally reduced to rGO.

2.3. Preparation of M-Bi/rGO/ZnO

Compared to traditional photochemical deposition using a single photoanode, M-Bi/rGO/ZnO were synthesized by a modified photochemical method via conducting the deposition in a short-circuited (SC) loop. A potassium-borate (K-Bi, 0.2 M) buffer solution was prepared from boric acid and the pH value was adjusted to 9.2 using a KOH solution. Then, Nickel nitrate hexahydrate or manganese nitrate tetrahydrate or cobalt chloride (1.0 mM) was prepared in the buffer solutions. After that, the solution was filtrated through a cellulose folded filter (Rotilabo, Typ 600P, 150 mm) and transferred to a quartz cell as the electrolyte. The prepared ZnO/rGO on FTO glass (1×1.5 cm^2) acted as the working photoelectrode, which was connected to a platinum (Pt) plate counter electrode (1.5×1.5 cm^2) to generate a SC loop. M-Bi layers (M = Ni, Co, Mn) in similar thicknesses were photo-deposited onto the rGO/ZnO to prepare M-Bi/rGO/ZnO, adopting the same deposition time under AM 1.5G simulated solar light with an output voltage of 1.5 μWcm^{-2}. For comparison, M-Bi/ZnO were synthesized by the similar method without rGO.

2.4. PEC measurement

Photoelectrochemical tests were carried out on a Zennium workstation (Zahner, Germany) in a three-electrode configuration, with a Ag/AgCl electrode as the reference electrode and a Pt plate (1.5×1.5 cm^2) as the counter electrode. FTO substrate (1×1 cm^2) deposited with catalysts acted as the working photoanodes. A K-Bi buffer solution (pH = 9.2) was adopted as the electrolyte and it is relatively stable with a sufficient proton-accepting capacity for M-Bi. All potentials were converted to RHE (reference hydrogen electrode) potentials. Before the tests, all the photoanodes were reconditioned (at 1.5 V) through the potentiostatic method. The current density-voltage (J-V) plots were obtained by the linear sweep voltammetry (LSV) method under irradiation of AM 1.5G simulated solar light (light intensity: 1 sun or 100 mW cm^{-2}) at 10 mV s^{-1}. Stability tests were performed using the photoanode (1×1.5 cm^2) as the working electrode by the potentiostatic measurements holding at 1.23 V for 2 h, during which the produced O_2 was monitored by a NeoFox Sport oxygen sensor (the details are provided in Supporting Information). Electrochemical impedance spectra (EIS) were examined under dark and light conditions from 100,000 to 0.1 Hz. Mott-Schottky measurements were also conducted in 0.2 M K-Bi solution (pH = 9.2) in dark at a frequency of 1000 Hz and a scanning rate of 10 mV s^{-1}. The charge carrier density (N_d) is calculated from the slopes of the plots using equation (1):[28]

$$N_d = (2/e\varepsilon_0\varepsilon)[d(1/C^2)/dV]^{-1} \quad (1)$$

where ε = 10 is the dielectric constant for ZnO,[29,30] ε_0 = 8.85×10^{-14} F/cm and e = 1.6 × 10^{-19} C.

To quantify the relationship between PEC performance and light absorption, incident photon-to-current conversion efficiencies (IPCE) were measured at 1.23 V under 1.5G simulated solar light in a Zahner Cimps system. The IPCE is derived from equation (2):

$$\text{IPCE} = (1240 \times \text{I})/(\lambda \times P_{light}) \quad (2)$$

here I (mA/cm^2) stands for the photocurrent density; λ (nm) is the incident light wavelength; and P_{light} (mW/cm^2) is the measured power density of monochromatic light at a specific wavelength.

3. Results and discussion

According to previous studies, M-Bi in high metal valence states were generally obtained by anodized electrodeposition or photo-induced chemical deposition.[7,8] Although they are amorphous materials, Ni-Bi, Ni-Pi, Co-Pi and Co-Bi thin films all contain ordered edge-sharing MO_6 clusters of molecular dimensions as active structure for OER. Nocera *et al.* reported that anodized Ni-Bi films possess edge-sharing NiO_6 octahedron layers in an ordered domain with diameters no less than 2 nm (~40 Ni centers).[7] According to X-ray pair distribution function (PDF) analysis, Co-Bi has a CoO(OH) structure with diminished coherence in the stacking direction.[8] In detail, it exhibits ordered domains of 3 - 4 nm composed by aligned layers of edge-shared CoO_6 octahedron clusters.[8] Based on the above findings, we built the models of NiO_6 (Fig. 1a) and CoO_6 (Fig. S1a) for Ni-Bi and Co-Bi, consisting of edge-sharing NiO_6 and CoO_6 octahedron clusters, respectively, which are far within the range of their ordered molecular domains. Borate species that are not the active sites for water oxidation were not included in the models. For Mn-Bi, it is unique and not previously studied. However, its structure is analogical to Mn-Pi as they are both manganese-oxide-based phases prepared in potassium-based buffer solutions (potassium borate or potassium phosphate). Bi and Pi mainly serve as proton-accepting bases in Mn-Bi or Mn-Pi structures. According to a recent study of Xi et al. by *in situ* soft X-ray Absorption Spectroscopy (XAS), electrodeposited MnPi contains both MnO_2 and birnessite.[31] They also reports that MnPi will transform into birnessite-type layer structure with increasing potential during anodic activation or in PEC process.[21,31] Birnessite will constitute a large part when Mn-Pi is used for electrocatalytic or PEC-OER test, which may apply equally to Mn-Bi. In addition, birnessite was generally proposed to be more active OER catalyst than MnO_2 in MnPi.[21,31,32] It is known that birnessite consists of edge-sharing MnO_6 octahedra layers with an interlayer of hydrated cations.[13] Hence, we construct active edge-sharing MnO_6 configuration (Fig. S1b), which allows for a reasonable comparison with NiO_6 and CoO_6. With the same active structures, their intrinsic OER kinetic activities can be compared in DFT calculations.

Typically, OER can be simulated by four elementary steps, where the intermediates of *OH, *O and *OOH are generated.

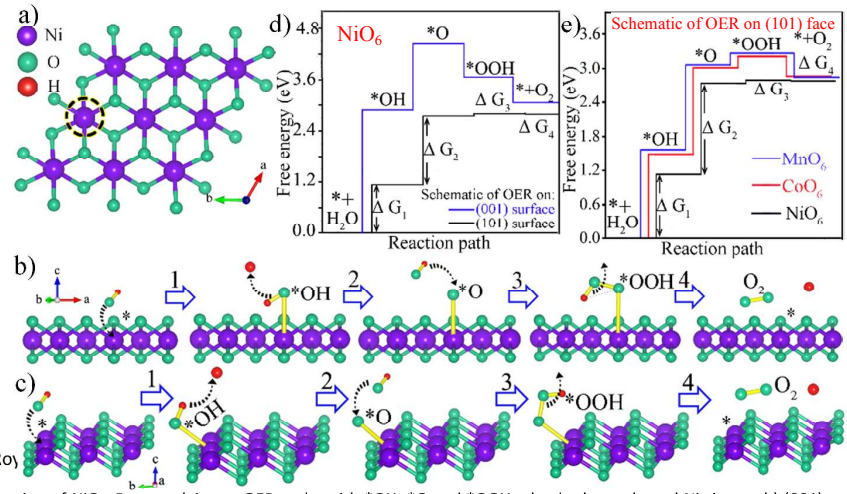

Fig. 1 a) Model configuration of NiO_6. Proposed 4-step OER paths with *OH, *O and *OOH adsorbed on selected Ni sites at b) (001) surface and c) (101) surface of NiO_6 (pH = 9.2). Diagrams of the 4-step Gibbs free energy changes calculated on d) (001) and (101) planes in NiO_6 and e) (101) surface for NiO_6, CoO_6, and MnO_6.

It is generally considered that (001) and (101) are exposed planes on the surface of M-Bi or M-Pi thin layers.[33] As OER tends to initiate from the surface sites of catalysts, we calculate the OER energy barriers for adsorption of *OH, *O and *OOH on these two main exposed surface planes, as described in Figs. 1b, 1c, S2, and S3. The energy barriers are associated with Gibbs free energy changes in the four steps (ΔG_1-ΔG_4), and the energy diagrams are obtained, as shown in Figs. 1d, 1e and S4. Due to the highest uphill/endothermic energy profiles from the deprotonation of H_2O ($*+H_2O \rightarrow *OH+H^++e^-$, step 1) and *OH ($HO* \rightarrow O*+H^++e^-$, step 2), step 1 or 2 is the rate-determining step. Step 3 ($*O+H_2O \rightarrow *OOH+H^++e^-$) requires relatively much lower energy barriers. The diagrams for step 4 ($*OOH \rightarrow O_2+H^++e^-$) are downhill/exothermic, suggesting that it is effortless to proceed. Figs. 1d and S4 show that a much lower Gibbs free energy is needed for step 1 and overall OER to occur on (101) surface than on (001) surface of MO_6. It is widely perceived that the adsorption of H_2O molecules and their decomposition into *OH in step 1 is highly critical in determining OER activity, since it is the initiation of OER on the surface of catalysts.[34] These results reveal that (101) plane is more active surface for OER. Therefore, we further compare OER kinetics on (101) planes of MO_6. The lowest overall uphill Gibbs free energy is observed in NiO_6, suggesting the lowest energy barrier for OER. The superiority of NiO_6 is mainly embodied in step 1 with a much smaller ΔG_1 value than CoO_6 and MnO_6, uncovering that it is much easier to initiate OER. To sum up, the DFT calculations reveal the lowest OER kinetics in NiO_6, followed by CoO_6, which is slightly better than MnO_6.

To verify DFT results and prepare highly efficient PEC devices, M-Bi (M = Ni, Co, Mn) thin-films were photodeposited onto rGO/ZnO photo-harvest configuration for PEC-OER tests. The preparation process of M-Bi/rGO/ZnO photoanodes is schematically described in Fig. 2a. Scanning electron microscopy (SEM) images (Fig. 2b and c) indicate that about 2 µm long ZnO NAs with diameters of 100 ~ 150 nm and smooth surfaces were vertically grown onto a FTO glass. Subsequently, graphene oxide (GO) was spin-coated onto the ZnO NAs, followed by an annealing process in N_2 flow for strong adhesion and reduction of GO to rGO. Figs. 2d and S5a show that gossamer-like rGO nanosheets cover the ZnO nanorods from the top or the side flexibly. Finally, M-Bi thin layers in similar thicknesses were uniformly deposited onto rGO/ZnO, turning the surfaces from smooth to rough (Figs. 2e, S5b, and S5c). To differentiate the individual role of rGO and M-Bi, M-Bi/ZnO were separately prepared without the deposition of rGO (Fig. S5d-f).

Transmission electron microscopy (TEM) images of rGO/ZnO show their good attachment (Fig. S6). Further, M-Bi layers (about 8 nm thick) attach tightly onto ZnO or rGO (Figs. 2f and S7-S9) after photodeposition. M-Bi/rGO/ZnO show similar high-resolution TEM (HRTEM) sturcture. Representative HRTEM images of Ni-Bi/rGO/ZnO (Fig. 2g) verify the amorphous nature of Ni-Bi with small ordered domains, which are also seen in Fig. S7. Clear lattice fringes corresponding to the (002) planes of hexagonal ZnO and the (002) planes of C

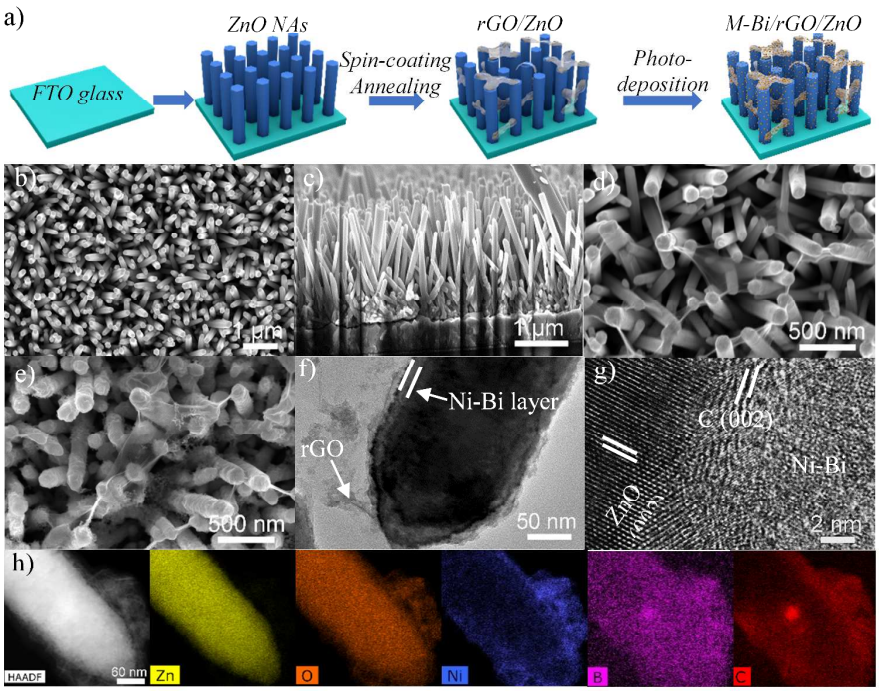

Fig. 2 a) Schematic fabrication procedure of M-Bi/rGO/ZnO composites. SEM images of b, c) ZnO NAs, d) rGO/ZnO and e) Ni-Bi/rGO/ZnO. f) TEM, g) HRTEM and h) the high angle annular dark field scanning TEM (HAADF-STEM) images with EDX elemental mapping results on Ni-Bi/rGO/ZnO.

are observed (Fig. 2g). The successful coating of Ni-Bi, Co-Bi and Mn-Bi on ZnO or rGO/ZnO can be clearly visualized by energy-dispersive X-ray spectroscopy (EDX) elemental mapping (Figs. 2h, S7c, S8c, and S9c).

Only reflection peaks of ZnO and FTO glass are detected in X-ray diffraction (XRD) patterns of M-Bi/rGO/ZnO composites, mainly due to the low loading amount of rGO and the amorphous nature of M-Bi thin layers (Fig. S10). X-ray photoelectron spectroscopy (XPS) was further conducted and the full spectra indicate the presence of M (M = Ni, Co, and Mn), Zn, B, C, K, and O on M-Bi/rGO/ZnO (Fig. S11). K arises from the buffer solution, which is intercalated in M-Bi films during the preparation.[7,8,21] The high-resolution spectra of Zn 2p, Ni 2p, Co 2p and Mn 2p are provided in Fig. S11b-e. The oxidation state of Zn is basically known as +2, while it is difficult for accurate determination of the oxidation states of Ni, Co and Mn from XPS spectra. According to previous literature results derived from *in situ* XAS analysis, the oxidation states of +2, +3, +4 coexist in Co of Co-Bi, Ni of Ni-Bi and Mn of Mn-Pi anodized thin films.[7,8,21,35] It is generally recognized that the average oxidation states of Ni, Co, Mn in M-Bi films prepared under applied potential or illumination are larger than 3,[7,8,21,35] due to the oxidization by applied potentials or photogenerated holes. This analysis also applies to M-Bi catalysts we prepared by photodeposition.

The PEC measurements were performed under one simulated sun illumination, using ZnO, rGO/ZnO, M-Bi/ZnO and M-Bi/rGO/ZnO current density of 0.26 mA cm^{-2} at 1.23 V (Fig. 3a). Once rGO is loaded onto ZnO, the photocurrent density (0.58 mA cm^{-2} at 1.23 V) is enlarged by a factor of 2.2, proving that rGO could remarkably inhibit electron-hole recombination and promote charge separation on ZnO. In contrast, when M-Bi overlayers are coated onto ZnO (M-Bi/ZnO) directly, the onset potentials exhibit desirable shifts in the cathodic direction (Fig. S12b), which confirms the function of M-Bi as efficient electrocatalysts. It was seen that rGO/ZnO displays a better charge mobility under the high voltage range, while M-Bi/ZnO show much more negative onset potentials. Therefore, rGO is believed to be essential for the photocurrent enhancement while M-Bi are more important for lowering OER kinetics. Generally consistent with DFT calculations, Ni-Bi with the lowest OER energy barrier presents the best catalytic performance and onset potential shifts by 0.12 V in the cathodic direction in Ni-Bi/ZnO, followed by Co-Bi/ZnO (0.08 V) and Mn-Bi/ZnO (0.03 V). In addition, the photocurrent densities are larger than that of ZnO (0.29, 0.32, and 0.38 mA cm^{-2} for Mn-Bi/ZnO, Co-Bi/ZnO and Ni-Bi/ZnO, respectively, at 1.23 V). For the ternary M-Bi/rGO/ZnO systems, both cathodically shifted onset potentials and largely increased current densities are observed owing to the synergistic effect of rGO, M-Bi with ZnO. Distinctly, Ni-Bi/rGO/ZnO is the best sample. Compared to ZnO, the onset potential migrates by 0.17 V in the cathodic direction (0.58 → 0.41 V) and the water oxidation photocurrent (0.86 mA cm^{-2} at 1.23 V) is enlarged by a factor of 3.3. By contrast, Co-Bi/rGO/ZnO delivers 0.12 V cathodic shift of the onset potential and photocurrent density of 0.80 mA cm^{-2} at 1.23 V. Mn-Bi/rGO/ZnO shows an inferior activity with 0.04 V onset potential shift and photocurrent density of 0.69 mA cm^{-2}. The

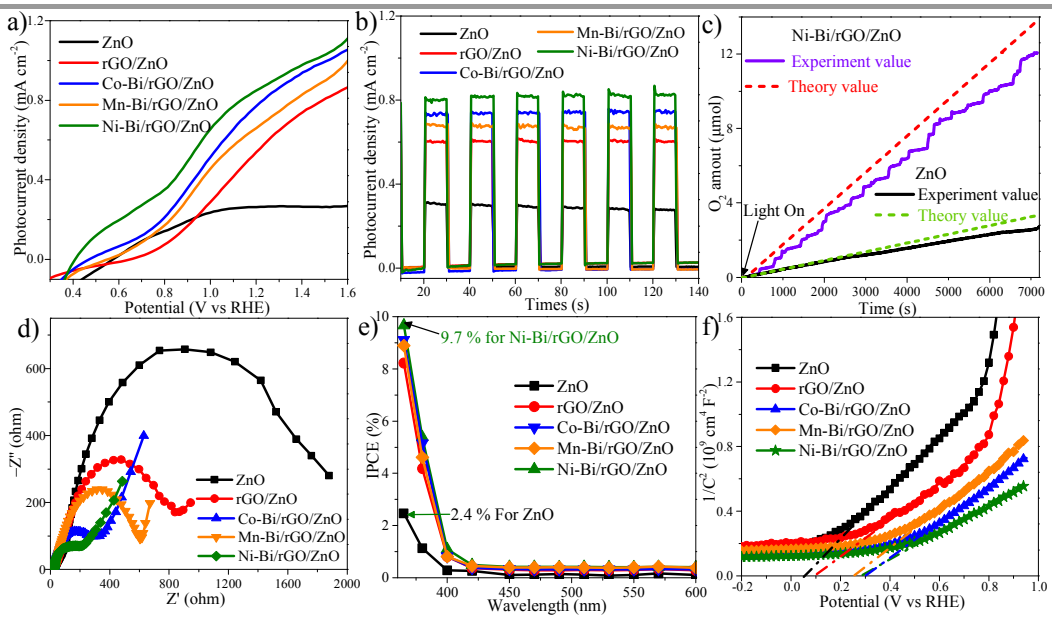

Fig. 3 a) J-V curves, b) I-t curves tested at 1.23 V under chopped light illumination, c) O_2 amount measured in real-time by an oxygen sensor (the dashed lines are the theoretical O_2 production calculated from the measured photocurrent), d) EIS measured under illumination, e) IPCEs of the photoanodes, and f) Mott-Schottky plots.

NAs as the photoanodes. The current density-voltage (J-V) plots of the samples under dark display low current densities (Fig. S12a). Upon irradiation, ZnO displays a limited PEC-OER activity with a photoresponse behavior of the photoanodes was further investigated by chronoamperometry (I-t) measurements under chopped light irradiations (Fig. 3b). In the ON-OFF irradiation cycles, prompt and

reproducible current responses are observed on all the samples. In high accordance with J-V tests, Ni-Bi/rGO/ZnO shows the highest photocurrent density of 0.8 mA cm^{-2} without attenuation, followed by Co-Bi/rGO/ZnO, Mn-Bi/rGO/ZnO, rGO/ZnO and ZnO. This PEC performance is among the superior values reported for ZnO based photoanodes, as compared in Table S1.

The stabilities of these photoanodes were evaluated by the potentiostatic measurements at 1.23 V (Fig. S13). Under irradiations, the photocurrent density of ZnO rapidly decays to 0.22 mA cm^{-2} (37% drop), while enhanced stability is observed on the M-Bi/rGO/ZnO composites (less than 9% recession). The rapid photocurrent decay of ZnO photoanode during the initial few minutes was possibly caused by the self-oxidative decomposition (also known as photocorrosion) of ZnO.[36] It was noted that compared with the smooth and straight surface of pristine ZnO NAs (Figs. 2a, b and S15a), the edges of some ZnO NAs were notched and corroded after the potentiostatic test (Figs. S14a, b and S15c). A thin shell was further observed on etched ZnO (Figs. S15d). As for the M-Bi/rGO/ZnO photoanodes, the initial rapid decrease of photocurrent might arise from the small amount of ZnO nanorods which were not covered by rGO or M-Bi. No appreciable changes were observed on SEM, HRTEM and EDS analysis of most Ni-Bi/rGO/ZnO nanorods (Figs. S14c, d and S16a), suggesting that the corrosion of ZnO by photo-induced holes was largely depressed.

In addition, the amount of O_2 evolution was real-time monitored on ZnO and Ni-Bi/rGO/ZnO during the stability tests (Fig. 3c). Comparing the theoretical O_2 production (calculated from the photocurrent) with the experimental values, the average faradic efficiencies of ZnO and Ni-Bi/rGO/ZnO were calculated to be around 90%. The high photocurrent-to-oxygen conversion efficiency highlights the efficient PEC water splitting process. It is proposed that a small portion of the obtained photocurrent in Ni-Bi/rGO/ZnO is created by oxidation of Ni, which is responsible for the gap between the theoretical and experimental O_2 evolution values. For ZnO, the 10% gap mainly originates from its photocorrosion. The amount of O_2 produced by Ni-Bi/rGO/ZnO is approximately 5 times larger than that of ZnO, confirming the largely enhanced OER efficiency of the ternary system.

Electrochemical impedance spectra (EIS) were examined on the photoanodes under both dark and light illuminations to investigate the charge transport properties at electrode/electrolyte interfaces. The semicircle diameters in low frequency region are related with interfacial charge transfer resistances (R_{ct}), which are critical in revealing the interfacial properties.[37,38] Compared to that tested in the dark (Fig. S17), R_{ct} values are drastically reduced under light irradiations (Fig. 3d). It was evidenced that the semicircle diameters (R_{ct}) of these photoanodes follows an increasing order as: Ni-Bi/rGO/ZnO < Co-Bi/rGO/ZnO < Mn-Bi/rGO/ZnO < rGO/ZnO < ZnO. Therefore, both rGO and M-Bi OECs can effectively accelerate the charge transport from the electrode to electrolyte by lowering electron transfer resistances. Consequently, the recombination rate of electron-hole pairs is reduced, making PEC water oxidation more efficient. Also, the accumulation of holes on ZnO is largely prevented, which inhibits its photocorrosion as stated in the stability test. Among these photoanodes, the Ni-Bi/rGO/ZnO shows the smallest semicircle diameter, indicating the fastest charge transfer kinetics as well as the highest photocurrent.

The optical properties of these samples were investigated by UV-vis diffuse reflectance spectroscopy (Fig. S18). Strong absorption in the UV-light region was observed on ZnO with a steep absorption edge at approximately 380 nm. The band gap was calculated to be 3.2 eV.[39] After being coupled with rGO and M-Bi, similar spectra were obtained, indicating that the deposition of rGO and M-Bi will not hinder the light absorption of ZnO. To further quantify the relationship between PEC performance and light absorption, incident photon-to-current efficiencies (IPCE) were measured on the electrodes. Consistent with the UV-vis spectra, Fig. 3e exhibits that all these photoanodes possess high photoconversion efficiencies in UV region (below 400 nm), yet little photoresponse in the visible-light region. The maximum IPCEs are obtained at 365 nm, which are 2.4%, 8.2%, 8.9%, 9.1% and 9.7% for ZnO, rGO/ZnO, Mn-Bi/rGO/ZnO, Co-Bi/rGO/ZnO and Ni-Bi/rGO/ZnO, respectively. Impressively, Ni-Bi/rGO/ZnO delivers an approximately 4 times higher photoelectroconversion efficiency than ZnO. This further confirms the synergistic contributions of rGO, M-Bi and ZnO to the final excellent PEC performance.

In Mott-Schottky plots (Fig. 3f), all the samples display positive slopes for n-type ZnO semiconductor as expected. The calculated charge carrier density (N_d) values for ZnO, rGO/ZnO, Co-Bi/rGO/ZnO, Mn-Bi/rGO/ZnO and Ni-Bi/rGO/ZnO are 0.9×10^{22}, 1.23×10^{22}, 1.26×10^{22}, 1.17×10^{22}, and 1.7×10^{22} cm^{-3}, respectively. The very slight change of N_d values indicates that the addition of M-Bi and rGO layers will not affect the doping level or carrier density within the ZnO electrode.[40,41] However, the flat band potentials (E_{fb}) obtained from the X-axis intercept display positive shifts after rGO and M-Bi introduction, suggesting decreased bending degrees of the band edges (as pointed by the red arrows in Fig. 4a).[40] This means that, although the bandgap of ZnO will not change, the valence band (VB) and conduction band (CB) shift towards positive positions (Fig. 4a). This change facilitates the charge transfer in ZnO and electrode/electrolyte interface and improves OER kinetics in the composites, leading to enhanced OER performance.[42]

The detailed PEC water oxidation process can be illustrated by proton-coupled electron transfer (PCET) process (Fig. 4a). In brief, electron-hole pairs are excited from ZnO under light radiation. With the assistance of conductive rGO nanosheets, the electrons can be efficiently separated to FTO glass and finally transferred to Pt counter electrode for proton reduction to H_2 via the external circuit, as shown in Fig. 4b. Meanwhile,

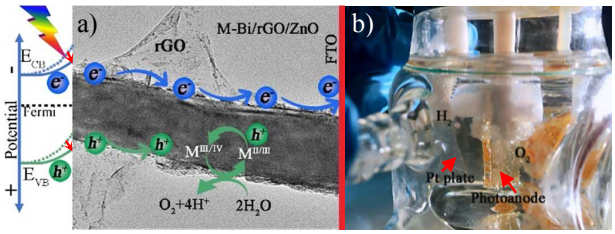

Fig. 4 a) A schematic illustration of the PEC water oxidation process in the M-Bi/rGO/ZnO photoanodes. b) Image of the photoelectrolytic cell during a PEC test.

the separated photo-induced holes and imposed anodic bias will oxidize $M^{II/III}$ centres to $M^{III/IV}$ for water oxidation to give O_2 at the electrode/electrolyte interface.[21,43,44] As this occurs, the $M^{III/IV}$ centres are reduced to $M^{II/III}$, which are rapidly reoxidized as $M^{III/IV}$ oxides by holes and anodic bias (known as the self-healing of M-Bi).[10,16] This redox reaction proceeds circularly for continuous water oxidation. It is worth noting that borate species ensure the long-term stability of M-Bi in water oxidation, by serving as a promulgator catalyst in PCET process and adsorbates of the active sites.[17]

Although the OER mechanism for M-Bi catalysts are all based on the PCET self-exchange reactions, they possess some imparities about active sites. It is vital to understand these differences to design more efficient catalysts. The experimental results indicate that Ni-Bi shows the best performance in improving OER kinetics of ZnO or rGO/ZnO photoanodes, followed by Co-Bi and Mn-Bi. This can be explained by both theoretical and experimental perspectives. DFT calculations compared the kinetic activity of the active structure (MO_6) in M-Bi, and the OER barriers followed the order as: NiO_6 < CoO_6 < MnO_6, especially in the first OER step, endowing Ni-Bi with kinetic advantages over Co-Bi and Mn-Bi. From experimental aspect, the better OER kinetics of Ni-Bi than Co-Bi and Mn-Bi can be supported by the lowest Tafel slope of Ni-Bi/rGO/ZnO, followed by Co-Bi/rGO/ZnO and Mn-Bi/rGO/ZnO (Fig. S19). Yogesh et al. also reported a lower Tafel slopes of Ni-Bi (30 mV/decade) than Co-Bi (52 mV/decade) in electrocatalytic OER.[45] Apart from the kinetic factor, the worst performance of Mn-Bi can be partially attributed to the existence of both MnO_2 and birnessite as aforementioned, whereas MnO_2 is not so active for OER.[21] Besides, previous studies suggest that Co^{IV}/Ni^{IV} are vital for efficient oxygen evolution on Co-Bi and Ni-Bi thin films,[7,8,46] while Mn^{III} sites (not Mn^{IV}) are consistently proposed as the active sites for OER of Mn-Pi or other manganese oxides recently.[21,47,48] However, during the PCET process, Mn^{III} species will be inevitably oxidized to Mn^{IV}, which impairs the OER performance of Mn-Bi. In this regard, designing Mn-based catalysts with valence states maintained at +3 will be valued to enhance their OER activities.

4. Conclusions

In summary, for the first time we explored and compared the OER catalytic abilities of M-Bi (M = Ni, Co, Mn) layers by theoretical and experimental investigations. The DFT calculations suggest that NiO_6 exhibits kinetic advantage over CoO_6 and MnO_6 with the lowest overall OER energy barrier. As beneficial OER catalysts, M-Bi were then successfully photocoated onto rGO/ZnO NAs whereby ZnO acts as a photo-harvester and rGO promotes efficient charge carrier separation. Consistent with the DFT results, Ni-Bi exhibits the best activity in improving OER kinetics, followed by Co-Bi and Mn-Bi. When the ternary composites (M-Bi/rGO/ZnO) were applied as photoanodes for PEC water oxidation, significantly enhanced performances were acquired. Distinctly, the onset potential of Ni-Bi/rGO/ZnO was shifted by 0.17 V in the cathodic direction and the photocurrent was enlarged by a factor of 3.3 (at 1.23 V) compared with ZnO. The photoelectroconversion efficiency of ZnO was elevated by about 4 times. This work generates new insights to the different metal-based complex systems for OER and provides an interesting direction in developing more efficient catalysts for feasible and cost-effective PEC water splitting.

Conflicts of interest

There are no conflicts to declare.

Acknowledgements

This work was supported by the Australian Research Council (DP150103026). Y. Li acknowledges the support from the NSFC (Grant No. 11674131). The authors acknowledge the help from the Centre for Microscopy, Characterization and Analysis (CMCA) of the University of Western Australia and the WA X-Ray Surface Analysis Facility of Curtin University funded by the Australian Research Council LIEF grant LE120100026 for material characterizations.

References

1 B. Dunn, H. Kamath and J. Tarascon, *Science*, 2011, **334**, 928–936.
2 J. Q. C. and C. L. T. Yao, X. An, H. Han, *Adv. Energy Mater.*, 2018, 1800210.
3 N. Armaroli and V. Balzani, *Chem. Eur.J.*, 2016, **22**, 32–57.
4 X. Li, S. Liu, K. Fan, Z. Liu, B. Song and J. Yu, *Adv. Energy Mater.*, 2018, 1800101.
5 I. Roger, M. A. Shipman and M. D. Symes, *Nat. Rev. Chem.*, 2017, **1**, 1–13.
6 M. Sarnowska, K. Bienkowski, P. J. Barczuk, R. Solarska and J. Augustynski, *Adv. Energy Mater.*, 2016, 1600526.
7 D. K. Bediako, B. Lassalle-Kaiser, Y. Surendranath, J. Yano, V. K. Yachandra and D. G. Nocera, *J. Am. Chem. Soc.*, 2012, **134**, 6801–6809.
8 C. L. Farrow, D. K. Bediako, Y. Surendranath, D. G. Nocera and S. J. L. Billinge, *J. Am. Chem. Soc.*, 2013, **135**, 6403–6406.
9 T. K. Townsend, E. M. Sabio, D. Browning and F. E. Osterloh, *Energy Environ. Sci.*, 2011, **4**, 4270–4275.
10 M. S. Faber and S. Jin, *Energy Environ. Sci.*, 2014, **7**,

3519–3542.
11 A. J. Esswein, Y. Surendranath, Y. Reece and D. G. Nocera, *Energy Environ. Sci.*, 2011, **4**, 499–504.
12 F. E. Osterloh, *Chem. Soc. Rev.*, 2013, **42**, 2294–2320.
13 K. P. Lucht and J. L. Mendoza-Cortes, *J. Phys. Chem. C*, 2015, **119**, 22838–22846.
14 M. Dinc, Y. Surendranath and D. G. Nocera, *Proc. Natl. Acad. Sci. U. S. A.*, 2010, **107**, 10337–10341.
15 Y. Surendranath, D. K. Bediako and D. G. Nocera, *Proc. Natl. Acad. Sci. U. S. A.*, 2012, **109**, 15617–15621.
16 D. A. Lutterman, Y. Surendranath and D. G. Nocera, *J. Am. Chem. Soc.*, 2009, **131**, 3838–3839.
17 D. K. Bediako, Y. Surendranath and D. G. Nocera, *J. Am. Chem. Soc.*, 2013, **135**, 3662–3674.
18 R. S. Khnayzer, M. W. Mara, J. Huang, M. L. Shelby, L. X. Chen and F. N. Castellano, *ACS Catal.*, 2012, **2**, 2150–2160.
19 Y. Bi, B. Zhang, L. Wang, Y. Zhang and Y. Ding, *Angew. Chemie Int. Ed.*, 2018, **57**, 2248–2252.
20 S. J. A. Moniz, J. Zhu and J. Tang, *Adv. Energy Mater.*, 2014, **4**, 1301590.
21 L. Xi, F. Wang, C. Schwanke, F. F. Abdi, R. Golnak, S. Fiechter, K. Ellmer, R. van de Krol and K. M. Lange, *J. Phys. Chem. C*, 2017, **121**, 19668–19676.
22 M. Fang, G. Dong, R. Wei and J. C. Ho, *Adv. Energy Mater.*, 2017, **7**, 1700559.
23 B. F. Zheng, T. Ouyang, Z. Wang, J. Long, Y. Chen and Z. Q. Liu, *Chem. Commun.*, 2018, **54**, 9583-9586.
24 H. M. Chen, C. K. Chen, Y. C. Chang, C. W. Tsai, R. S. Liu, S. F. Hu, W. S. Chang and K. H. Chen, *Angew. Chem., Int. Ed.*, 2010, **122**, 6102–6105.
25 W. Geng, X. Zhao, H. Liu and X. Yao, *J. Phys. Chem. C*, 2013, **117**, 10536–10544.
26 Ellen M. P. Steinmiller and Kyoung-Shin Choi, *PNAS*, 2009, **106**, 20633–20636.
27 W. S. Hummers and R. E. Offeman, *J. Am. Chem. Soc.*, 1958, **80**, 1339.
28 W. Li, P. Da, Y. Zhang, Y. Wang, X. Lin, X. Gong and G. Zheng, *ACS Nano*, 2014, **8**, 11770–11777.
29 I. Mora-Seró, F. Fabregat-Santiago, B. Denier, J. Bisquert, R. Tena-Zaera, J. Elias and C. Lévy-Clément, *Appl. Phys. Lett.*, 2006, **89**, 1–4.
30 R. Bin Wei, P. Y. Kuang, H. Cheng, Y. B. Chen, J. Y. Long, M. Y. Zhang and Z. Q. Liu, *ACS Sustainable Chem. Eng.*, 2017, **5**, 4249–4257.
31 L. Xi, C. Schwanke, J. Xiao, F. F. Abdi, I. Zaharieva and K. M. Lange, *J. Phys. Chem. C*, 2017, **121**, 12003–12009.
32 D. M. Robinson, Y. B. Go, M. Mui, G. Gardner, Z. Zhang, D. Mastrogiovanni, E. Garfunkel, J. Li, M. Greenblatt and G. C. Dismukes, *J. Am. Chem. Soc.*, 2013, **135**, 3494–3501.
33 H. Kim, J. Park, I. Park, K. Jin, S. E. Jerng, S. H. Kim, K. T. Nam and K. Kang, *Nat. Commun.*, 2015, **6**, 8253.
34 Y. Sun, S. Gao, F. Lei, J. Liu, L. Liang and Y. Xie, *Chem. Sci.*, 2014, **5**, 3976–3982.
35 L. Xi, C. Schwanke, D. Zhou, D. Drevon, R. Van De Krol and K. M. Lange, *Dalt. Trans.*, 2017, **46**, 15719–15726.
36 X. Li, S. Liu, K. Fan, Z. Liu, B. Song and J. Yu, *Adv. Energy Mater.*, 2018, **8**, 1–7.
37 S. Hernández, D. Hidalgo, A. Sacco, A. Chiodoni, A. Lamberti, V. Cauda, E. Tresso and G. Saracco, *Phys. Chem. Chem. Phys.*, 2015, **17**, 7775–7786.
38 D. Fan, C. Guo, H. Ma, D. Zhao, Y. Li, D. Wu and Q. Wei, *Biosens. Bioelectron.*, 2016, **75**, 116–122.
39 P. Y. Kuang, J. R. Ran, Z. Q. Liu, H. J. Wang, N. Li, Y. Z. Su, Y. G. Jin and S. Z. Qiao, *Chem. Eur.J.*, 2015, **21**, 15360–15368.
40 T. W. Kim and K.-S. Choi, *Science*, 2014, **343**, 990–994.
41 F. Ning, M. Shao, S. Xu, Y. Fu, R. Zhang, M. Wei, D. G. Evans and X. Duan, *Energy Environ. Sci.*, 2016, **9**, 2633–2643.
42 P. Y. Kuang, Y. Z. Su, K. Xiao, Z. Q. Liu, N. Li, H. J. Wang and J. Zhang, *ACS Appl. Mater. Interfaces*, 2015, **7**, 16387–16394.
43 M. W. Kanan, J. Yano, Y. Surendranath, M. Dincă, V. K. Yachandra and and D. G. Nocera, *J. Am. Chem. Soc.*, 2010, **132**, 13692–13701.
44 K.-H. Ye, Z. Wang, J. Gu, S. Xiao, Y. Yuan, Y. Zhu, Y. Zhang, W. Mai and S. Yang, *Energy Environ. Sci.*, 2017, **10**, 772–779.
45 Y. Surendranath, D. K. Bediako and D. G. Nocera, *Proc. Natl. Acad. Sci. U. S. A.*, 2012, **109**, 15617–15621.
46 M. D. Symes, Y. Surendranath, D. A. Lutterman and D. G. Nocera, *J. Am. Chem. Soc.*, 2011, **133**, 5174–5177.
47 Morgan Chan, D. A. Kitchaev, J. Nelson Weker, C. Schnedermann, K. Lim, G. Ceder, W. Tumas, M. F. Toney and D. G. Nocera, *Proc. Natl. Acad. Sci.*, 2018, **115**, 5261-5268.
48 M M. Najafpour and A.N.Moghaddam, *Dalt. Trans.*, 2012, **41**, 10292–10297.

Table of contents

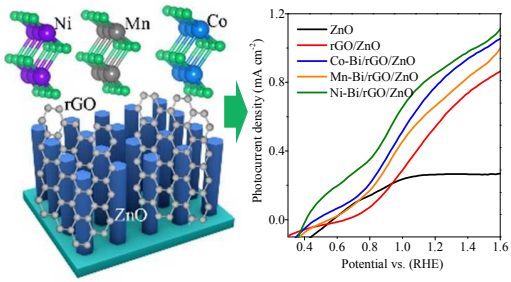

The activity of Ni, Co, or Mn-based oxygen-evolving catalysts is screened and M-Bi/rGO/ZnO photoanodes are demonstrated for photoelectrochemical water splitting

Supporting Information

A Comparative Study of Metal (Ni, Co, or Mn)-Borate Catalysts and Their Photodeposition on rGO/ZnO Nanoarrays for Photoelectrochemical Water Splitting

Huayang Zhang,[‡ab] Wenjie Tian,[‡a] Yunguo Li,[‡c] Hongqi Sun,*[b] Moses O. Tadé[a] and Shaobin Wang*[a]

[a] *WA School of Mines: Minerals, Energy and Chemical Engineering, Curtin University, GPO Box U1987, WA 6845, Australia. E-mail: shaobin.wang@curtin.edu.au*

[b] *School of Engineering, Edith Cowan University, 270 Joondalup Drive, Joondalup, WA 6027, Australia. E-mail: h.sun@ecu.edu.au*

[c] *Department of Earth Sciences, University College London, Gower Street, London WC1E 6BT, United Kingdom.*

[‡] These a*uthors contributed equally.*

1. Simulation details

We performed spin-polarized DFT calculations in order to elucidate the OER activities of M-Bi (M = Ni, Co, Mn). We used the Vienna *Ab initio* Simulations Package (VASP)[1,2] and projected augmented wave (PAW)[3–5] method for total energy calculations. In the calculations, 3*d* and 4*s* electrons were treated as valence electrons for Ni, Co and Mn, and 2*s* and 2*p* for O. The exchange-correlation interaction was treated with Generalized gradient approximation (GGA) parameterized by Perdew, Burke and Ernzerhof (PBE).[6] For strongly localized *d* electrons, the GGA has systematic and noncancelling errors.[7] So, we adopted GGA+U[8] to correct the self-interaction error and overdelocalized *d* states. The effective U_{eff} introduced by Dudarev et al.[8] was used with 5.25, 4.5 and 5.5 eV for Ni,[8] Co,[9] and Mn,[10] respectively.

We started from relaxing bulk MO_2 (space group $R\bar{3}m$, No. 166) composed of MO_6 octahedra. The cutoff energy of plane-wave basis was set to 520 eV, and integrations over the first Brillouin zone were made using Gamma-centred k-point sets of 8×8×8. With these settings, the total energy was able to converge within 1 meV/atom. Atomic positions were fully relaxed with the energy converged within 10^{-6} eV/cell and the force converged to less than 10^{-4} eV/Å. Then, we relaxed the (100) surface with a single layer of MO_6 octahedra spaced by 17 Å. The

(101) zigzag ribbons were also relaxed in slab calculations. The same cutoff energy and similar k-point grids as dense as in the bulk calculations (in the case of vacuum direction, only Gamma point was used) were used for slab calculations. The detailed treatment of OER free energy calculations can be found in our previous publication.[11]

2. Materials characterizations

X-ray diffraction spectra were recorded on an Empyrean multi-purpose research diffractometer (Panalytical Empyrean XRD) using the filtered Cu Kα radiation (λ = 1.5418 Å) with an accelerating voltage of 40 kV and a current of 40 mA. The transmission electron microscopy (TEM) images were obtained on a JEOL 2100 TEM microscope (120 kV) and FEI TITAN G2 (200 kV). The high angle annular dark field scanning transmission electron microscopy (HAADF-STEM) images and EDX mapping analysis were carried out on FEI TITAN G2 (200 kV). X-ray photoelectron spectroscopy (XPS) was conducted under ultrahigh vacuum condition on a Kratos Axis Ultra DLD system. UV-visible diffuse reflectance spectra were collected on a Cary 100 UV-visible spectrophotometer (Agilent, US).

3. Real-time oxygen measurements

An oxygen sensor (Ocean Optics, Neofox, FOSPOR-R 1/16) was inserted into the photoelectrolytic glass cell to probe the produced O_2 concentration via the fluorescence quenching method during the stability test. The glass cell has a quartz window (the volume of the headspace was 30 mL, excluding the space occupied by the septum, oxygen sensor, and the solution). The needle probe was inserted into the 1/16" threaded holes through a rubber septum and conducted uninterrupted O_2 readings at 5 s intervals throughout the test. Ahead of the detection, the probe was calibrated through a 2-point method, with a reading error of 1%. Before irradiation, the reactor was purged with N_2 for 10 min to exclude air in the reaction system. The test started from 10 min baseline reading followed by 100 min irradiation under AM 1.5G simulated solar light (light intensity: 1 sun or 100 mW cm^{-2}) with the potentiostatic method (at 1.23 V vs. RHE).

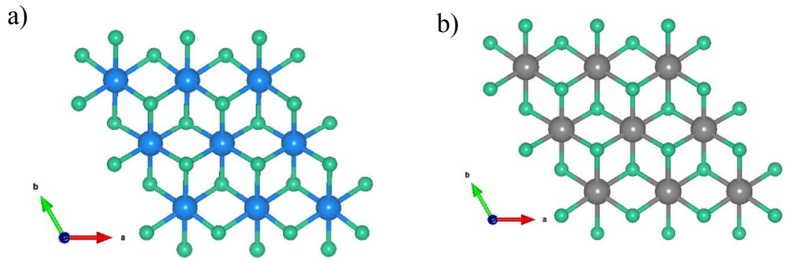

Fig. S1 Model structures for a) CoO_6 and b) MnO_6.

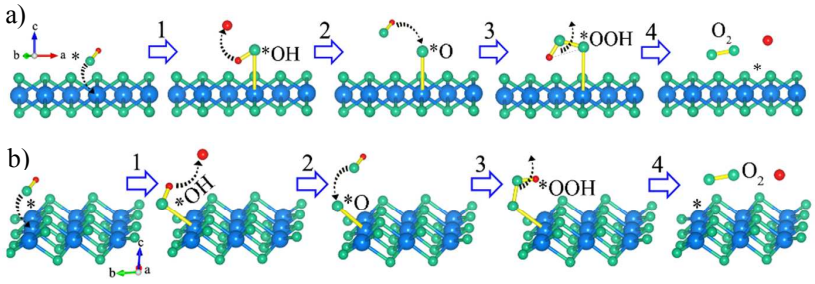

Fig. S2 Proposed 4-step OER paths with *OH, *O and *OOH adsorbed on selected Co sites at a) (001) surface and b) (101) surface of CoO_6 (pH = 9.2).

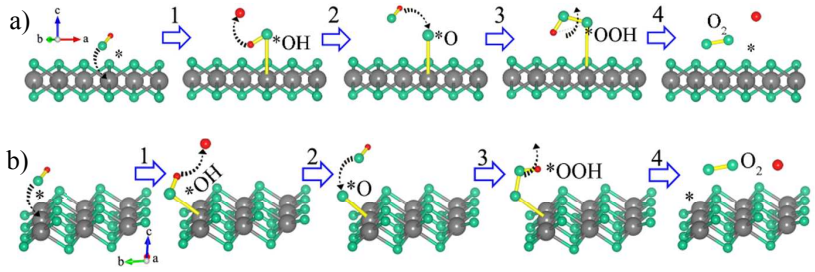

Fig. S3 Proposed 4-step OER paths with *OH, *O and *OOH adsorbed on selected Co sites at a) (001) surface and b) (101) surface of MnO_6 (pH = 9.2).

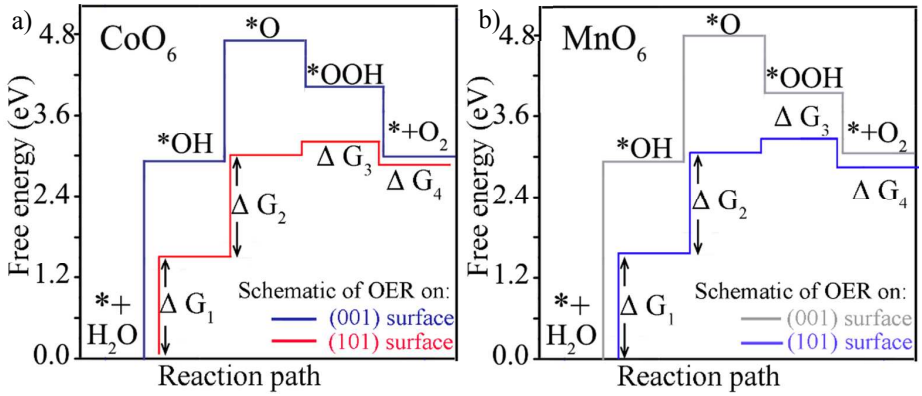

Fig. S4 Diagrams of the 4-step Gibbs free energy changes calculated on the (001) surface and (101) surface in a) CoO_6 and b) MnO_6.

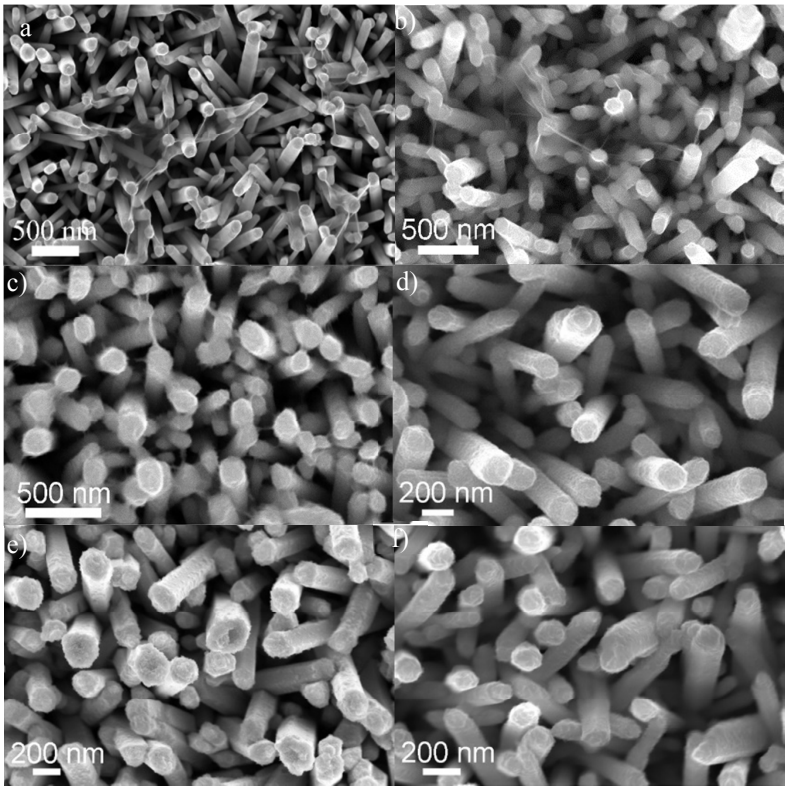

Fig. S5 SEM images of a) rGO/ZnO, b) Co-Bi/rGO/ZnO, c) Mn-Bi/rGO/ZnO, d) Ni-Bi/ZnO, e) Co-Bi/ZnO and f) Mn-Bi/ZnO.

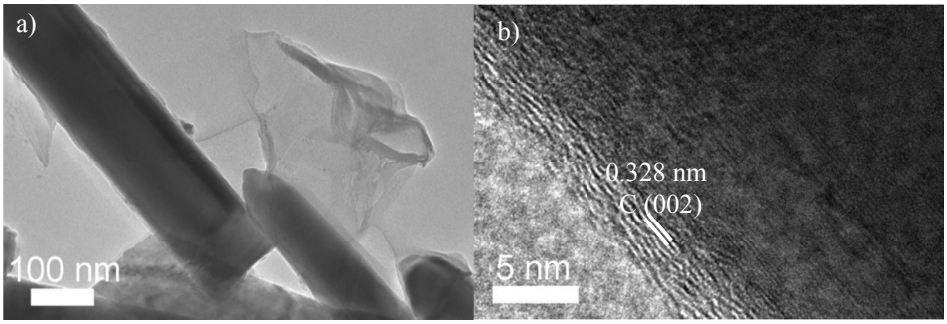

Fig. S6 a) TEM and b) HRTEM images of rGO/ZnO.

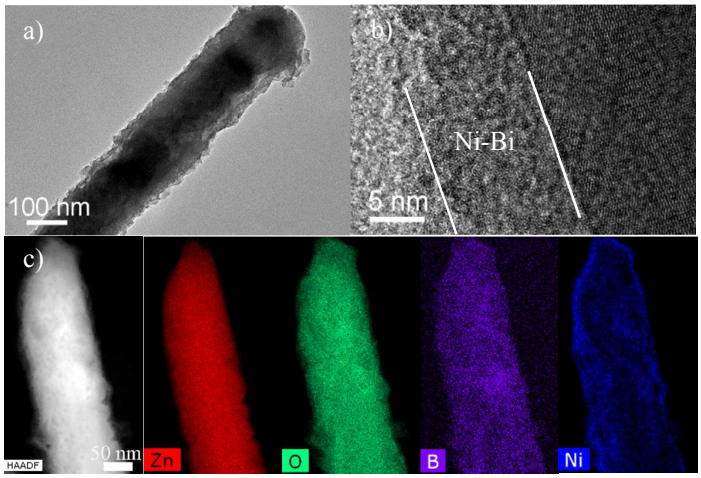

Fig. S7 a) TEM, b) HRTEM and c) HAADF-STEM with EDX mapping images of Ni-Bi/ZnO.

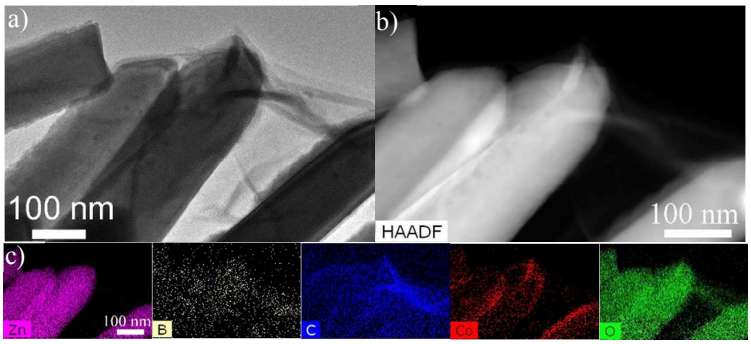

Fig. S8 a) TEM, b) HAADF-STEM and c) EDX mapping images of Co-Bi/rGO/ZnO.

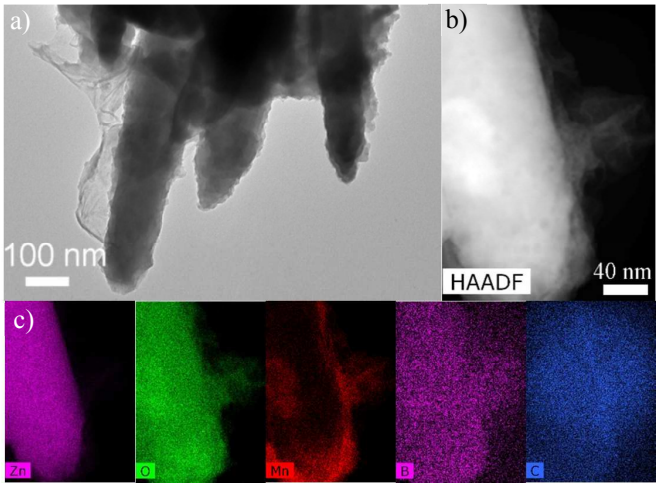

Fig. S9 a) TEM, b) HAADF-STEM and c) EDX mapping images of Mn-Bi/rGO/ZnO.

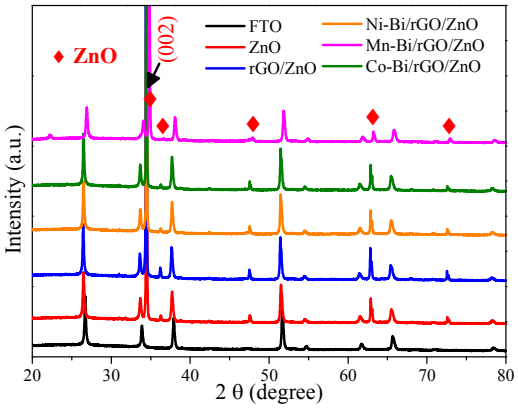

Fig. S10 XRD patterns of FTO substrate, ZnO, rGO/ZnO and M-Bi/rGO/ZnO.

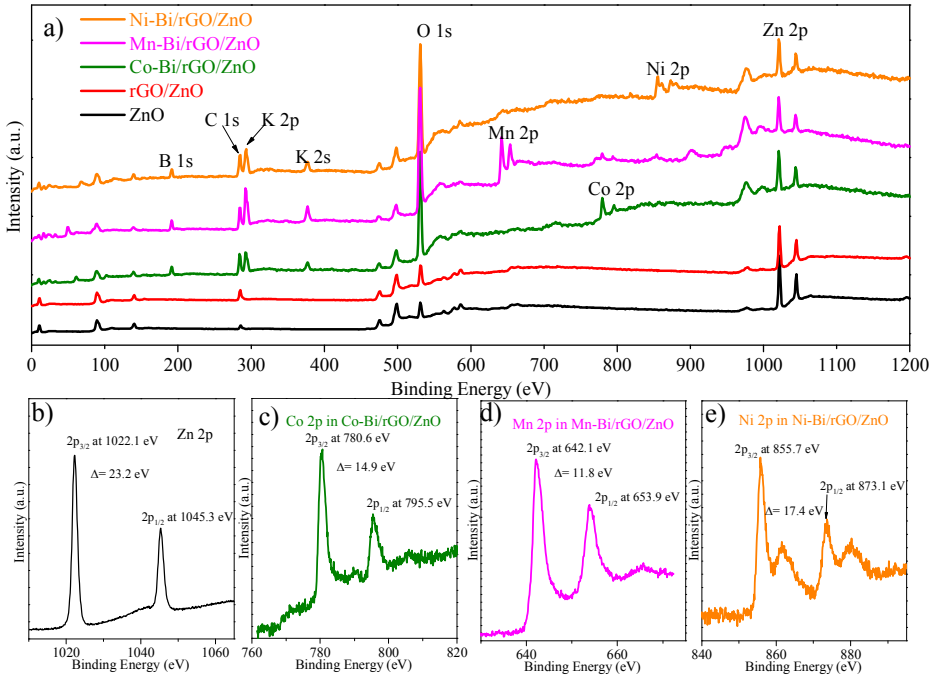

Fig. S11 a) Full XPS spectra of the samples and high-resolution spectra of b) Zn 2p, c) Co 2p, d) Mn 2p and e) Ni 2p.

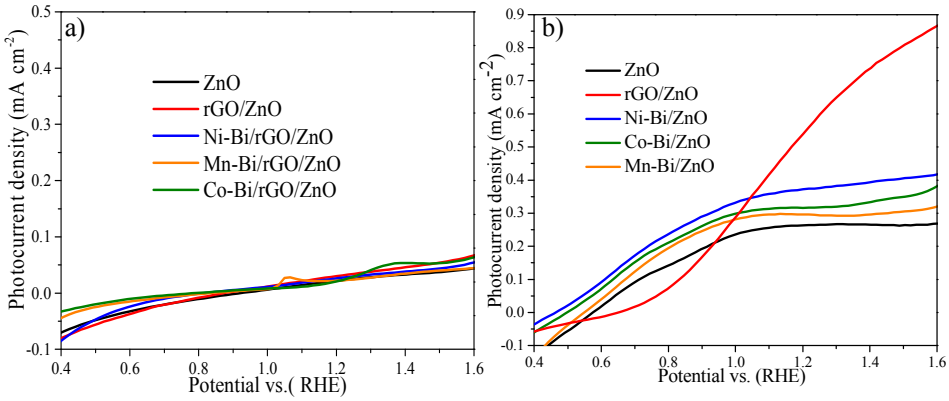

Fig. S12 J-V curves tested on ZnO, rGO/ZnO, and M-Bi/ZnO under a) dark condition and b) irradiation.

In dark condition (Fig. S12a), the small peaks observed on Mn-Bi/rGO/ZnO (at 1.05 V) and Co-Bi/rGO/ZnO (at 1.4 V) were caused by the valence state changes of Mn and Co species due to the oxidation.[12,13]

Table S1. A comparison of the PEC performance of Ni-Bi/rGO/ZnO with previously reported ZnO-based catalysts for water oxidation in a mild medium under light intensity of 100 mW cm^{-2}.

Photoanode	Photocurrent density (potentials vs. RHE)	Testing condition	Reference
C-doped ZnO	1.00 mA cm^{-2} at 1.61 V	0.5 M Na_2SO_4	14
Au NP/$ZnFe_2O_4$/ZnO	1.1 mA cm^{-2} at 1.4 V	0.5 M Na_2SO_4	15
3D ZnO/TiO_2/FeOOH NWs	1.59 mA cm^{-2} at 1.8 V	0.5 M Na_2SO_4	16
$Ni(OH)_2$/ZnO NR	~0.90 mA cm^{-2} at 1.2 V	0.5 M Na_2SO_4	17
Au-ZnO nanopencil	~1.5 mA cm^{-2} at 1.6 V	0.5 M Na_2SO_4	18
ZnO-Au-SnO_2 nanorods	0.08 mA cm^{-2} at 1.4 V	0.5 M Na_2SO_4	19
(N-GQDs)/ZnO nanowire	~0.6 mA cm^{-2} at 1.63 V	0.5 M Na_2SO_4	20
CdS/RGO/ZnO Nanowire	0.8 mA cm^{-2} at 1.63 V	0.1 M phosphate buffer solution	21
Three-dimensional ZnO nanoforests	0.919 mA cm^{-2} at 1.81 V	0.5 M Na_2SO_4	22
Au-ZnO Nanowire	1.3 mA cm^{-2} at 1.6 V	0.5 M Na_2SO_4	23
ZnO-IrOx nanorod	0.7 mA cm^{-2} at 1.2 V	0.25M Na_2SO_4	24
Ni-Bi/rGO/ZnO	1.15 mA cm^{-2} at 1.6 V	0.2 M K-Bi	This work

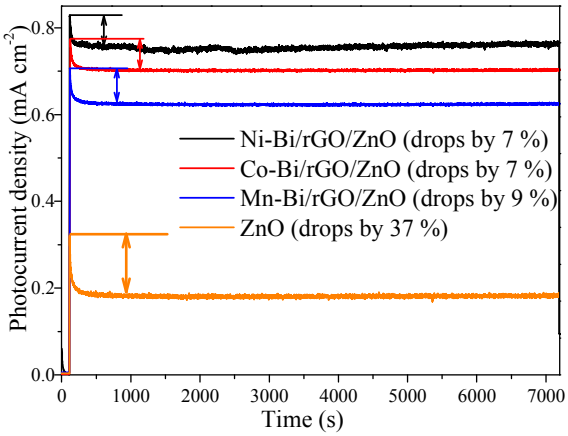

Fig. S13 Potentiostatic measurements (at 1.23 V vs RHE) of ZnO and M-Bi/rGO/ZnO.

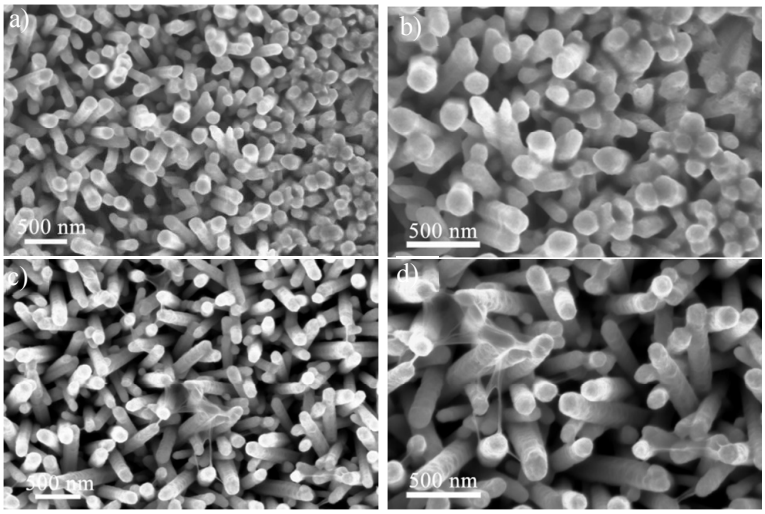

Fig. S14 SEM images of a, b) ZnO and c, d) Ni-Bi/rGO/ZnO after potentiostatic measurements.

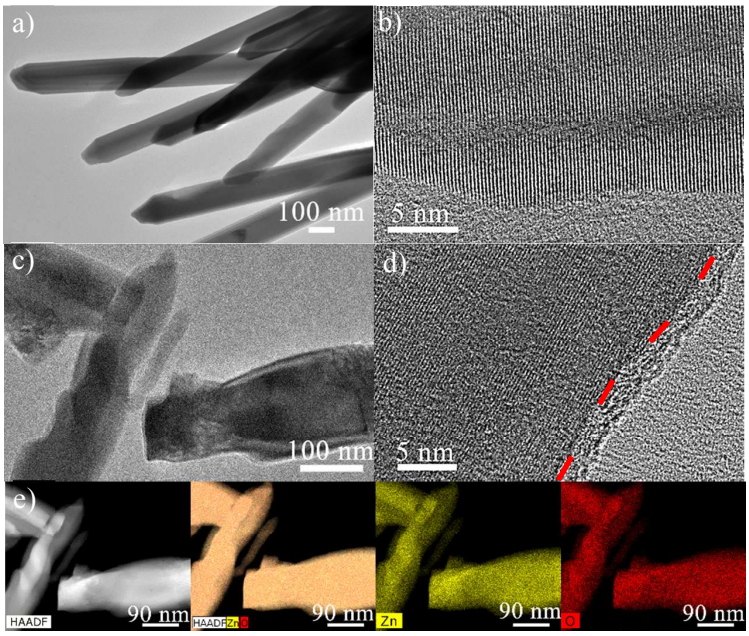

Fig. S15 a) TEM and b) HRTEM images of pristine ZnO. c) TEM, d) HRTEM and e) HAADF-STEM with corresponding EDS mapping images of ZnO after the potentiostatic measurement.

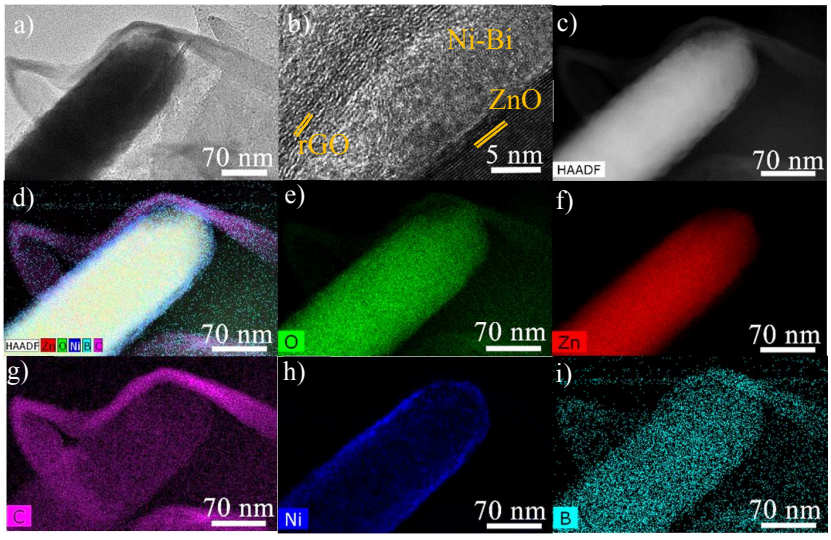

Fig. S16 a) TEM, b) HRTEM, c) HAADF-STEM, and d-i) EDS mapping images of Ni-Bi/rGO/ZnO after the potentiostatic measurement.

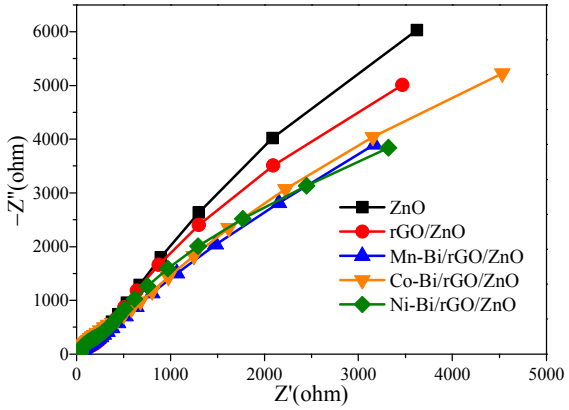

Fig. S17 Electrochemical impedance spectra (EIS) measured in dark.

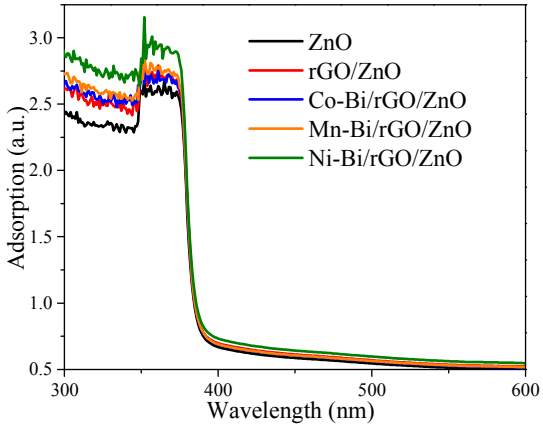

Fig. S18 UV-vis diffuse reflectance spectra of ZnO, rGO/ZnO and M-Bi/rGO/ZnO.

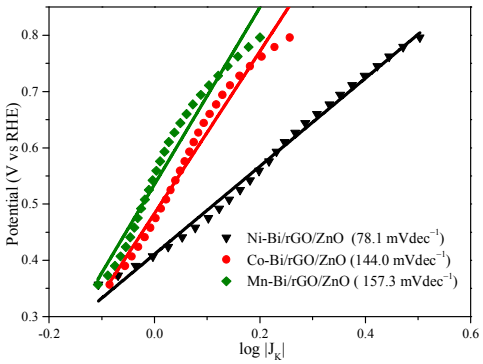

Fig. S19 Tafel plots for M-Bi/rGO/ZnO.

REFERENCES

1 G. Kresse and D. Joubert, *Phys. Rev. B*, 1999, **59**, 1758–1775.

2 P. E. Blöchl, *Phys. Rev. B*, 1994, **50**, 17953–17979.
3 G. Kresse and J. Furthmüller, *Comput. Mater. Sci.*, 1996, **6**, 15–50.
4 G. Kresse and J. Furthmüller, *Phys. Rev. B*, 1996, **54**, 11169–11186.
5 G. Kresse and J. Hafner, *Phys. Rev. B*, 1993, **48**, 13115–13118.
6 J. P. Perdew, K. Burke and M. Ernzerhof, *Phys. Rev. Lett.*, 1996, **77**, 3865–3868.
7 Y. Li, Y.-L. Li, B. Sa and R. Ahuja, *Catal. Sci. Technol.*, 2017, **7**, 545–559.
8 S. Dudarev and G. Botton, *Phys. Rev. B - Condens. Matter Mater. Phys.*, 1998, **57**, 1505–1509.
9 C. Ling, L. Q. Zhou and H. Jia, *RSC Adv.*, 2014, **4**, 24692–24697.
10 D. A. Tompsett, D. S. Middlemiss and M. S. Islam, *Phys. Rev. B - Condens. Matter Mater. Phys.*, 2012, **86**, 1–8.
11 H. Zhang, W. Tian, Y. Li, H. Sun, M. O. Tade and S. Wang, *J. Mater. Chem. A*, 2018, **6**, 6265–6272.
12 C. Gandolfi, T. Cotting, P. N. Martinho, O. Sereda, A. Neels, G. G. Morgan and M. Albrecht, *Dalt. Trans.*, 2011, **40**, 1855–1865.
13 R. S. Khnayzer, M. W. Mara, J. Huang, M. L. Shelby, L. X. Chen and F. N. Castellano, *ACS Catal.*, 2012, **2**, 2150–2160.
14 D. A. Links, *Nanoscale*, 2012, **4**, 6515–6519.
15 A. Sheikh, A. Yengantiwar, M. Deo and S. Kelkar, *Small*, 2013, **9**, 2091–2096.
16 Z. Li, S. Feng, S. Liu, X. Li, L. Wang and W. Lu, *Nanoscale*, 2015, **7**, 19178–19183.
17 Y. Mao, H. Yang, J. Chen and J. Chen, *Nano Energy*, 2014, **6**, 10–18.
18 J. Gong, *Nanoscale*, 2014, **7**, 77–81.
19 J. Li, H. Cheng, Y. Chiu and Y. Hsu, *Nanoscale*, 2016, **8**, 15720–15729.
20 Z. Zeng, F. Xiao, X. Gui, R. Wang, T. Thatt and Y. Tan, *J. Mater. Chem. A*, 2016, **4**, 16383–16393.
21 K. Zhao, X. Yan, Y. Gu, Z. Kang, Z. Bai, S. Cao, Y. Liu, X. Zhang and Y. Zhang, *Small*, 2016, **12**, 245–251.
22 V. A. Online, *Nanoscale*, 2014, **6**, 8769–8780.
23 C. E. T. Al, *ACS Nano*, 2012, **6**, 7362–7372.
24 D. Shao, Y. Cheng, J. He, D. Feng, L. Zheng, L. Zheng, X. Zhang, J. Xu, W. Wang, W. Wang, F. Lu, H. Dong, L. Li, H. Liu, R. Zheng and H. Liu, *ACS Catal.*, 2017, **7**, 5308–5315.